REPORT DOCUMENTATION PAGE

Form Approved OMB NO. 0704-0188

1. REPORT DATE (DD-MM-YYYY)	2. REPORT TYPE	3. DATES COVERED (From - To)
26-11-2018	Final Report	15-Aug-2017 - 14-May-2018

4. TITLE AND SUBTITLE
Final Report: Solar Blind Sn-alloyed Ga2O3 Schottky Photodetectors

5a. CONTRACT NUMBER
W911NF-17-1-0377

5b. GRANT NUMBER

5c. PROGRAM ELEMENT NUMBER
611102

6. AUTHORS

5d. PROJECT NUMBER

5e. TASK NUMBER

5f. WORK UNIT NUMBER

7. PERFORMING ORGANIZATION NAMES AND ADDRESSES
University of Central Florida
12201 Research Parkway, Suite 501

Orlando, FL 32826 -3246

8. PERFORMING ORGANIZATION REPORT NUMBER

9. SPONSORING/MONITORING AGENCY NAME(S) AND ADDRESS (ES)
U.S. Army Research Office
P.O. Box 12211
Research Triangle Park, NC 27709-2211

10. SPONSOR/MONITOR'S ACRONYM(S)
ARO

11. SPONSOR/MONITOR'S REPORT NUMBER(S)
71602-EL-II.2

12. DISTRIBUTION AVAILIBILITY STATEMENT
Approved for public release; distribution is unlimited.

13. SUPPLEMENTARY NOTES
The views, opinions and/or findings contained in this report are those of the author(s) and should not contrued as an official Department of the Army position, policy or decision, unless so designated by other documentation.

14. ABSTRACT

15. SUBJECT TERMS

16. SECURITY CLASSIFICATION OF:			17. LIMITATION OF ABSTRACT	15. NUMBER OF PAGES	19a. NAME OF RESPONSIBLE PERSON
a. REPORT	b. ABSTRACT	c. THIS PAGE			Winston Schoenfeld
UU	UU	UU	UU		19b. TELEPHONE NUMBER 407-823-6898

RPPR Final Report
as of 26-Nov-2018

Agency Code:

Proposal Number: 71602ELII **Agreement Number: W911NF-17-1-0377**
INVESTIGATOR(S):

Name: Winston Schoenfeld
Email: winston@creol.ucf.edu
Phone Number: 4078236898
Principal: Y

Organization: **University of Central Florida**
Address: 12201 Research Parkway, Suite 501, Orlando, FL 328263246
Country: USA
DUNS Number: 150805653 EIN: 592924021
Report Date: 14-Aug-2018 Date Received: 26-Nov-2018
Final Report for Period Beginning 15-Aug-2017 and Ending 14-May-2018
Title: Solar Blind Sn-alloyed Ga2O3 Schottky Photodetectors
Begin Performance Period: 15-Aug-2017 **End Performance Period:** 14-May-2018
Report Term: 0-Other
Submitted By: Winston Schoenfeld Email: winston@creol.ucf.edu
Phone: (407) 823-6898
Distribution Statement: 1-Approved for public release; distribution is unlimited.

STEM Degrees: 0 **STEM Participants:** 0

Major Goals: See attached PDF.

Accomplishments: See attached PDF.

Training Opportunities: See attached PDF.

Results Dissemination: See attached PDF.

Honors and Awards: See attached PDF.

Protocol Activity Status:

Technology Transfer: See attached PDF.

PARTICIPANTS:

Participant Type: Postdoctoral (scholar, fellow or other postdoctoral position)
Participant: Partha Mukhopadhyay
Person Months Worked: 9.00 **Funding Support:**
Project Contribution:
International Collaboration:
International Travel:
National Academy Member: N
Other Collaborators:

CONFERENCE PAPERS:

RPPR Final Report
as of 26-Nov-2018

Publication Type: Conference Paper or Presentation **Publication Status:** 1-Published
Conference Name: Oxide-based Materials and Devices IX
Date Received: 26-Nov-2018 Conference Date: 27-Jan-2018 Date Published:
Conference Location: San Francisco, United States
Paper Title: Tin-gallium-oxide-based UV-C detectors
Authors: Partha Mukhopadhyay, Mykyta Toporkov, Winston V. Schoenfeld
Acknowledged Federal Support: **Y**

ARO STIR Final Progress Report

Submitted by: Dr. Partha Mukhopadhyay and Dr. Winston V. Schoenfeld
CREOL, The College of Optics and Photonics
University of Central Florida

Project Title: STIR: Solar Blind Sn-Alloyed Ga_2O_3 Schottky Photodetectors
Contract Number: W911NF-17-1-0377
Period of Performance: 15 August 2017 – 14 May 2018
Program Manager: Dr. Mike Gerhold

Table of Contents

TABLE OF CONTENTS 1
KEY STIR PROJECT ACCOMPLISHMENTS 2
PROJECT OVERVIEW 2
SUMMARY OF RESULTS 3
Thrust 1: Dependence of Sn incorporation on MBE growth conditions 3
SGO growth on Sapphire Substrates 3
SGO Epitaxy on Ga_2O_3 Substrates 5
Thrust 2: Fabrication of functional SGO detectors on sapphire and native Ga_2O_3 substrates 6
SGO on sapphire (MSM Devices) 6
SGO on β-Ga_2O_3 (Schottky Devices) 6
Thrust 3: Characterization of fabricated devices 7
SGO on sapphire (MSM Devices) 7
SGO on β-Ga_2O_3 (Schottky Devices) 11
IMPROVED GROWTH CONDITIONS AND RESULTANT IMPACT 14
Improved MSM Devices (on Sapphire) 14
Improved Schottky Devices (on Bulk β-Ga_2O_3) 16
COMPARISON OF BEST RESULTS 17
CONCLUSIONS 19
APPENDIX 1: SUMMARY OF UV DETECTOR PERFORMANCES 20
APPENDIX 2: SUMMARY OF EPITAXIAL SAMPLES GROWN FOR THIS PROJECT 22
BIBLIOGRAPHY 24

Key STIR Project Accomplishments

1. MBE growth of $(Sn_xGa_{1-x})_2O_3$ on both sapphire and bulk β-Ga_2O_3 substrates was successfully demonstrated.
2. Tunability of the SGO bandgap was demonstrated by adjustment of the Sn concentration in the alloy, allowing for adjustment from 240-270nm.
3. Functional MSM and Schottky devices were successfully fabricated on sapphire and β-Ga_2O_3 substrates, respectively.
4. MSM devices realized peak responsivities as high as 16.8 A/W at 258 nm, representing a quantum efficiency of 80. Passivation by SiN was found to offer a 10X improvement in responsivity, increasing the peak responsivity realized to 64.7 A/W.
5. Schottky devices realized peak responsivities as high as $1.15x10^4$ A/W at -5V, representing a quantum efficiency of 58,605. ***__***This is the highest reported responsivity for a planar Ga_2O_3 based UV-C detector to our knowledge***__. Increasing the reverse bias to -20V increased the responsivity to a record $7.4x10^4$ A/W.
6. Determined that SiN passivation of MSM devices results in a 10x increase in the responsivity, warranting further development and optimization.
7. Project was successful in demonstrating the feasibility of tunable MSM and Schottky detectors in the UV-C spectral region using SGO.

Project Overview

Solar blind UV photodetectors with a cutoff wavelength below ~280 nm and are of a great interest for variety of military and civilian applications such as missile interception, non-line-of-sight communication, flame sensing, and air/water purification. Wide bandgap alloy systems such as $Mg_xZn_{1-x}O$ and $Al_xGa_{1-x}N$ have been widely studied and developed for solar blind applications. However, increasing the content of Mg ($x > 0.33$)[1] or Al ($x>0.45$)[2] in these ternaries to achieve true solar blind response is accompanied by issues such as phase segregation in MgZnO and film quality deterioration in AlGaN. Therefore, despite the maturity of these ternaries, it is of interest to identify alternative compounds that might provide a less challenging path to competitive solar blind devices. β-Ga_2O_3 has recently attracted a great interest in the scientific community due to its high bandgap (~4.9eV), n-type doping capabilities, and high breakdown electric field of 8 MV/cm[3, 4], making it a promising alternative. Additionally, bulk undoped and n-doped, single crystal β-Ga_2O_3 substrates can be grown by a variety of crystal growth methods such as float zone (FZ)[5], edge-defined film-fed growth[6, 7], and the Czochralski process[8]. Such substrates are expected to be scalable and inexpensive, as is the case for current sapphire substrates. In fact, already single-crystal β-Ga_2O_3 substrates of up to 4-inch-diameter have been demonstrated[6], creating the pathway for the availability of inexpensive native substrates. This, in turn, provides a viable native substrate for the growth of high quality homoepitaxial β-Ga_2O_3 films that can be fabricated into vertical Schottky diode photodetectors for zero bias operation, such as depicted in Figure 1.

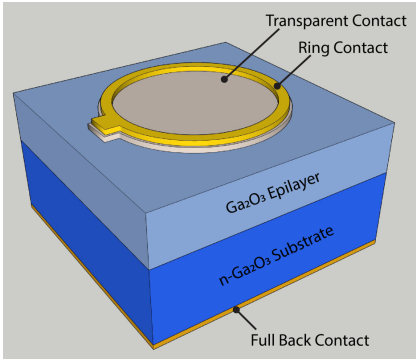

Figure 1: Basic Ga_2O_3 Schottky detector device structure.

One shortcoming of homoepitaxial β-Ga_2O_3 for solar blind applications is its short wavelength band edge of ~240 nm (E_g~4.9 eV)[9], lying just below the ideal cutoff wavelength of

around 275nm. One potential mitigation pathway is alloying with a lower bandgap oxide. Rutile Tin Oxide (SnO_2) has a band gap of ~3.6 eV, offering the potential of alloying with β-Ga_2O_3 to enable band gap tunability in the UV-C region. Tin doping and alloying have been shown to decrease resistivity to 0.1 Ω-cm and lower bandgap of β-Ga_2O_3[10]; however, high content Sn-alloyed Ga_2O_3 (SGO) detectors have not been investigated through molecular beam epitaxy (MBE).

The primary objective of this STIR is to demonstrate the feasibility of Sn-alloyed Ga_2O_3 ($(Sn_xGa_{1-x})_2O_3$ *or* SGO) Schottky photodetectors, providing the foundation that justifies considering the approach for future device development/demonstration funding. The project contained three major technical task areas: (1) Identifying the dependence of Sn incorporation in Gallium Oxide on MBE growth conditions, (2) Fabrication of functional $(Sn_xGa_{1-x})_2O_3$ detectors on sapphire and native Ga_2O_3 substrates, and (3) Characterization of fabricated devices.

Summary of Results

As noted above, the STIR project contained three major task areas. The following subsections provide a summary of the key results within each.

Thrust 1: Dependence of Sn incorporation on MBE growth conditions

SGO growth on Sapphire Substrates

This first thrust aimed to determine if controllable alloying of Tin in Ga_2O_3 is possible by MBE and to determine the tunability potential of the SGO alloy. For this work, SGO epilayers were grown on sapphire substrates using conditions similar to that we use for Ga_2O_3 epitaxy. Initial efforts utilized a fixed gallium cell temperature at 880˚C, with Sn incorporation being varied by adjusting the Sn cell temperature. Figure 2 provides a summary of the transmission data for various SGO epilayers. To our surprise, we did not observe measurable band edge shifting with increasing Sn cell temperature, even with various Ga and Sn cell temperatures and flux ratios as noted in the right side of Figure 2.

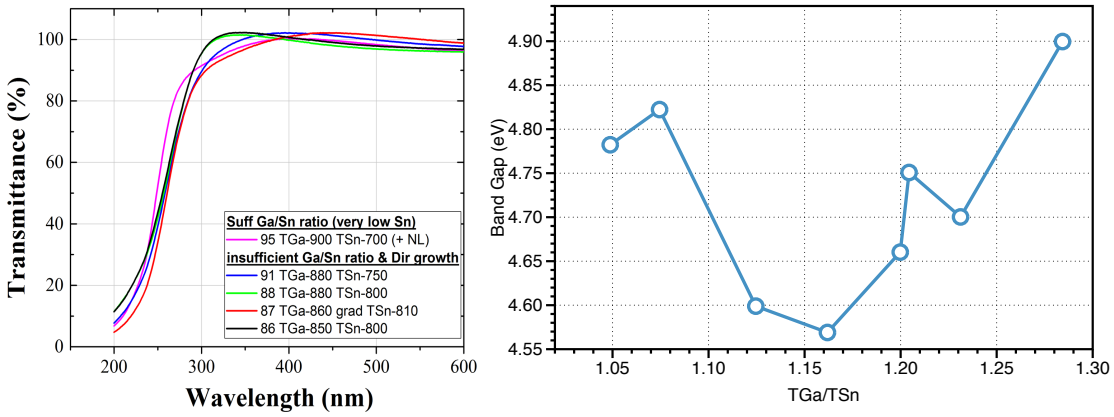

Figure 2: Transmission data (left) and band gap (right) determined from Tauc plots for SGO epilayers.

Upon further investigation we discovered an interesting dependence of Sn incorporation on the Ga flux. We observed that Sn incorporation is only adjustable through changes in Sn flux when a sufficient Ga flux is provided. When growing with a Ga cell temperature of 850-880˚C, Sn incorporation is limited to only a few percent, irrespective of Sn cell temperature (see Figure 2 above). However, when we increased the Ga flux by increasing the source temperature to 900˚C, we were able to tune Sn incorporation by adjusting the Sn cell temperature as demonstrated by the shift in transmission and energy gap in Figure 3.

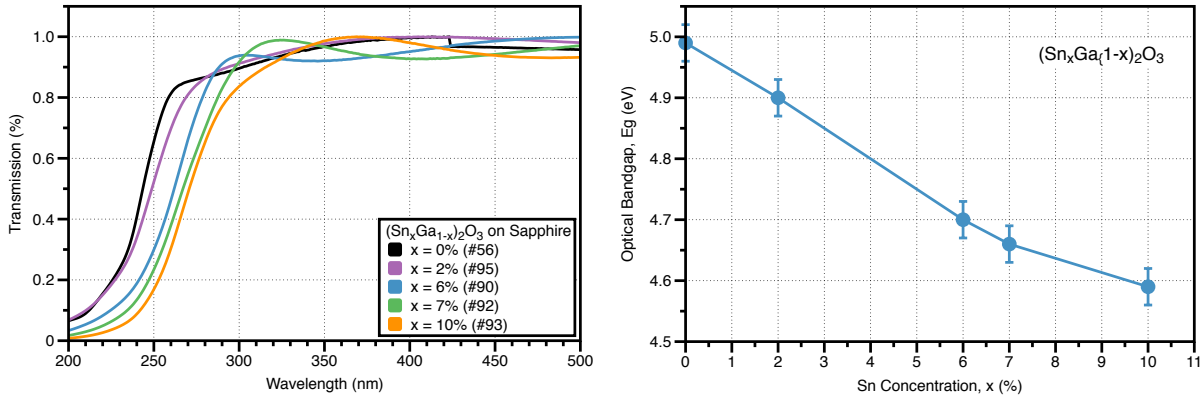

Figure 3: Transmission data and Tauc plots for SGO epilayers with sufficient Ga flux (left) and optical bandgap determined from Tauc plot.

By adjusting the Sn cell from 700-830˚C, we were able to adjust the Sn incorporation from x = 2 to 10%, resulting in a shift of the optical bandgap from 4.9eV (x=2%) down to 4.59eV (x=10%), as determined by Tauc plot analysis, shown in the right of Figure 3. In this region, the bandgap follows a nearly linear trend of:

$$E_g(x_{Sn}) = 4.977 - 0.0419 \cdot x_{Sn}$$

While the fit follows the data quite well, it should be noted that this linear fit is not appropriate for the entire alloy range since it would predict a bandgap for SnO_2 of ~0.8 eV that is well below the known value of 3.6 eV. This is to be expected given that β-Ga_2O_3 has a monoclinic crystal structure and SnO_2 is rutile. As will be demonstrated later, Sn substitutionally incorporates into the Ga_2O_3 lattice, maintaining the monoclinic crystal structure for the compositional range we studied ($0.0 < x < 0.3$), and thus fitting of the bandgap as a function of Sn concentration results in a prediction of the "monoclinic" tin oxide alloy for 100% Sn.

We have carried out X-Ray diffraction (XRD) on these initial epilayers to determine what phases are present. Figure 4 (left) provides the XRD data from the TGO epilayer and confirms the presence of the β-phase Ga_2O_3, as evidenced by the (-201), (-402), and (-603) peaks in the data. XRD does not show the presence of tin oxide inclusions, confirming the substitutional incorporation of tin to the lattice of β-Ga_2O_3. Figure 4 (right) shows the secondary ion mass spectrometry (SIMS) depth profiles for TGO epilayers on sapphire grown at various Sn cell temperatures, demonstrating the ability to adjust Sn content. Furthermore, AFM measurements reveal a RMS roughness on the order of 2 nm, consistent with the RHEED observations during MBE growth.

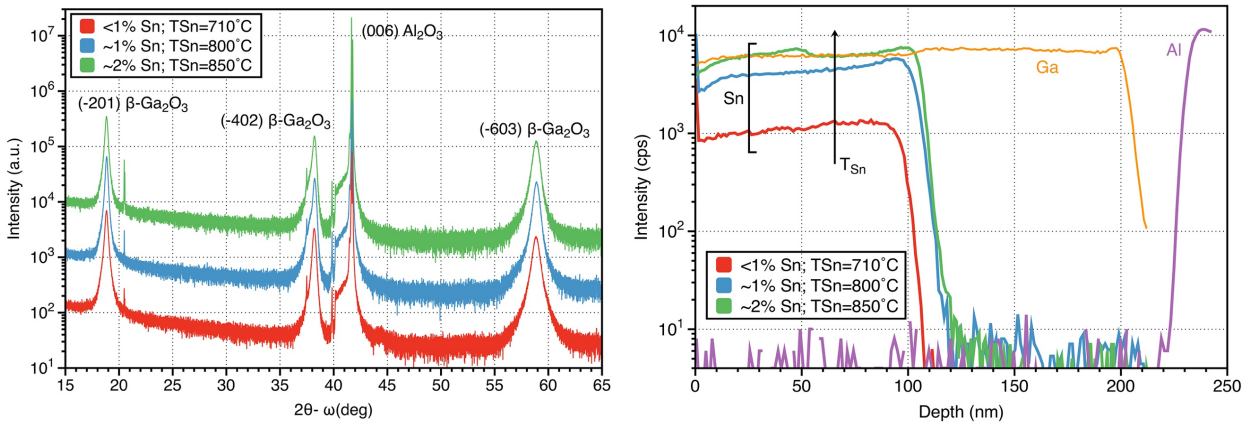

Figure 4: XRD data (left) and SIMS depth profiles (right) for three SGO epilayers of varying Sn concentration.

SGO Epitaxy on Ga_2O_3 Substrates

Prior to moving forward to device demonstration we needed to verify that the SGO growth conditions used for Sapphire substrates was transferrable to native n-type β-Ga_2O_3 substrates. Using our sapphire based growth conditions, we grew four samples on n-type β-Ga_2O_3 and tested their XRD. The Omega-2θ XRD scans for the four samples are provided in Figure 5 (a). Clear in the XRD are the (020), (203), and (-801) peaks from the β-Ga_2O_3 substrate, as well as a (113) peak at ~59.5˚ that originates from the SGO epilayer. We observed a systematic shift in the (113) peak position to lower angle with increasing Sn concentration that corresponds to an increase in (113) lattice d-spacing for higher Sn concentrations, as demonstrated in Figure 5 (b and c).

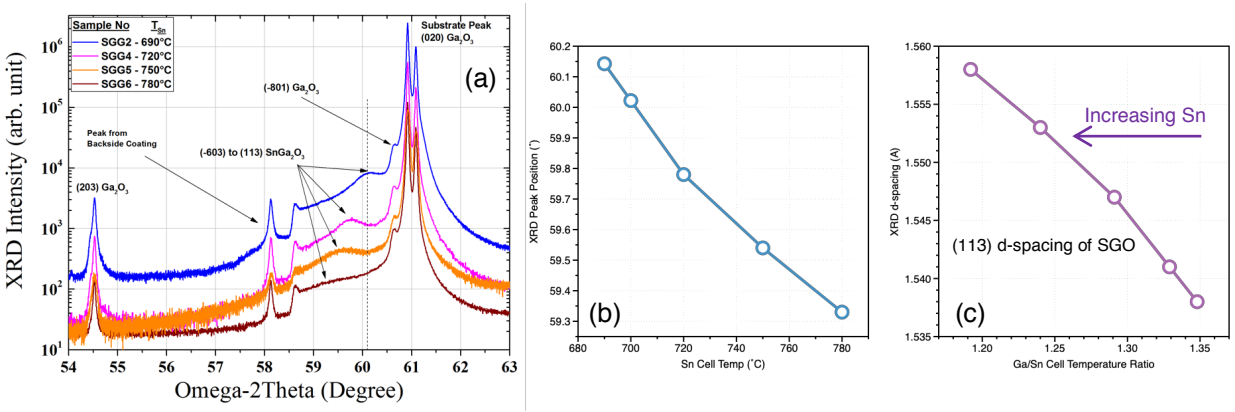

Figure 5: XRD data (a) for SGO epilayers on n-type Ga_2O_3 substrates, (b) observed shift of SGO (113) peak, and (c) d-spacing as a function of Sn concentration.

Based on this work, we are confident that SGO alloys are capable of enabling band gap tuning of Ga_2O_3 to longer wavelengths across the upper UV-C region and into the UV-B range. Upon this successful demonstration of functional band gap tuning through Sn alloying, we then proceeded to the second thrust of the project, the fabrication of functional UV-C detectors from the epilayers.

Thrust 2: Fabrication of functional SGO detectors on sapphire and native Ga_2O_3 substrates

The next thrust of the program was to fabricate functional devices from the SGO epilayers to determine their suitability for MSM and Schottky UV-C detectors. In this STIR project, both MSM and Schottky detectors were fabricated, with MSM detectors utilizing SGO epilayers on sapphire substrates and Schottky detectors using SGO epilayers grown on n-type β-Ga_2O_3 substrates. The following two subsections provide details on the MSM and Schottky device fabrication.

SGO on sapphire (MSM Devices)

MSM devices were fabricated using a single step photolithography process for metal contact lift-off. Shipley 1813 positive photoresist was spun on the sample, exposed using our MSM device photomask, and then developed in 351 developer at a 4:1 (H_2O:351) ratio. Figure 6 provides a basic cross-section of the MSM devices, showing the Ni/Au top contact fingers used for photocurrent collection.

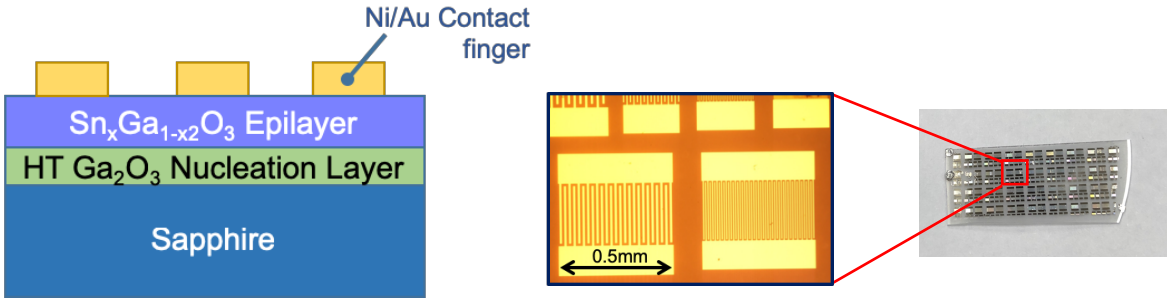

Figure 6: SGO MSM device cross-section schematic (left) and fabricated devices (right).

There were no adhesion issues or fabrication challenges encountered for the SGO on sapphire structures, and large areas of functional devices were easily realized with a standard photolithography liftoff process. The measured properties of the devices are presented later in the Thrust 3 section.

SGO on β-Ga_2O_3 (Schottky Devices)

Similar to the SGO on sapphire, devices were fabricated using a standard photolithography process. Given that the β-Ga_2O_3 substrates are conductive, vertical Schottky devices were possible. Figure 7 shows the basic structure of the Schottky SGO devices.

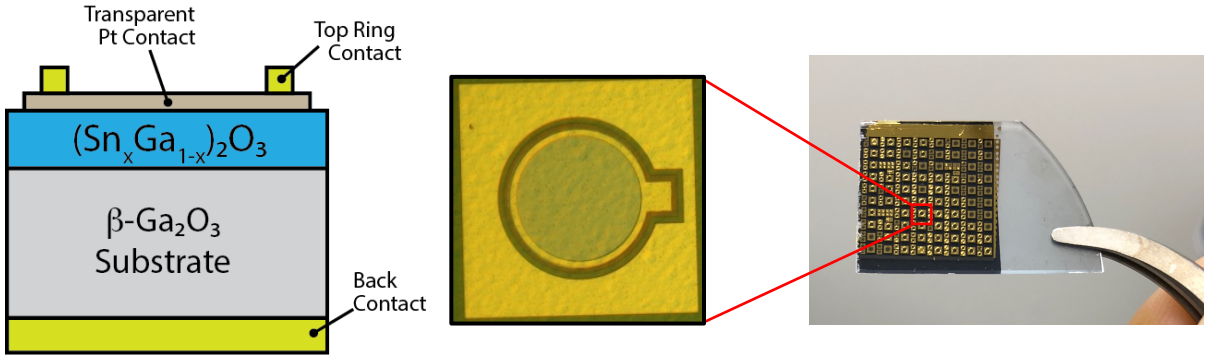

Figure 7: SGO Schottky device cross-section schematic (left) and fabricated devices (right).

A Ti/Al/Ni (20nm/100nm/50nm) back contact was formed on the rear side of the β-Ga_2O_3 substrate, annealed at 500˚C for 60 sec. The front side consisted of two steps: (1) deposition of a Pt high work function (ϕ_m ~ 5.5 eV) semitransparent layer (~ 3 nm), and (2) subsequent deposition of a thick Ni/Au ring contact. The thin Pt semitransparent contact enables light transmission from the top side of the device while still providing a suitable Schottky barrier. We have not optimized the thickness of this Pt layer to date – clearly reducing its thickness would increase the transparency of the layer to UV-C illumination, but at the consequence of reduced conductivity. We expect the thickness of the Pt can be reduced further to increase device responsivity. For the samples, two basic device sizes are present, large and small with a diameter of 500μm and 300μm, respectively.

Thrust 3: Characterization of fabricated devices

SGO on sapphire (MSM Devices)

We first tested the dark and light I-V characteristics of the MSM devices. These are presented in Figure 8 for both a Ga_2O_3 (no Sn) and $(Sn_{0.06}Ga_{0.94})_2O_3$ device.

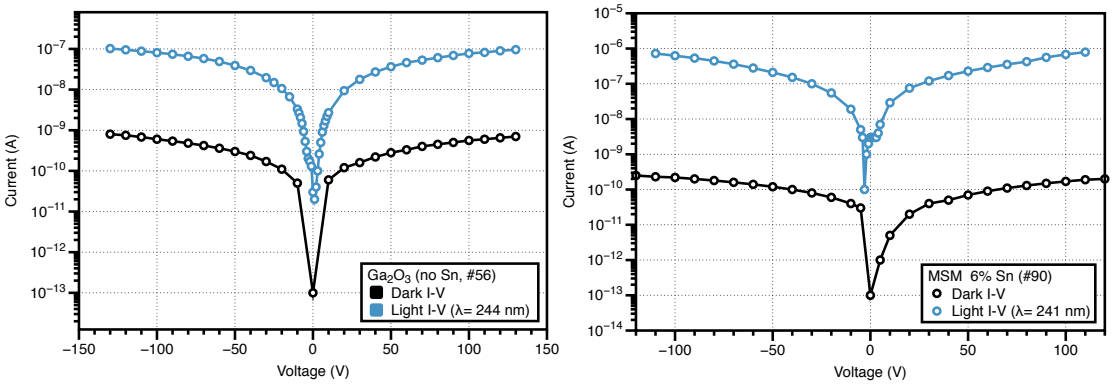

Figure 8: Dark and Light I-V characteristics for Ga_2O_3 (left) and 6% SGO (right) MSM devices.

The I-V characteristics follow the expected symmetrical behavior about the zero-voltage point. Over the entire voltage range tested, the dark current of both devices is in the pA regime. Upon

illumination with UV light (241nm or 244 nm), both devices show strong increases due to generated photocurrent that is 2 to 3 orders of magnitude higher than the dark current.

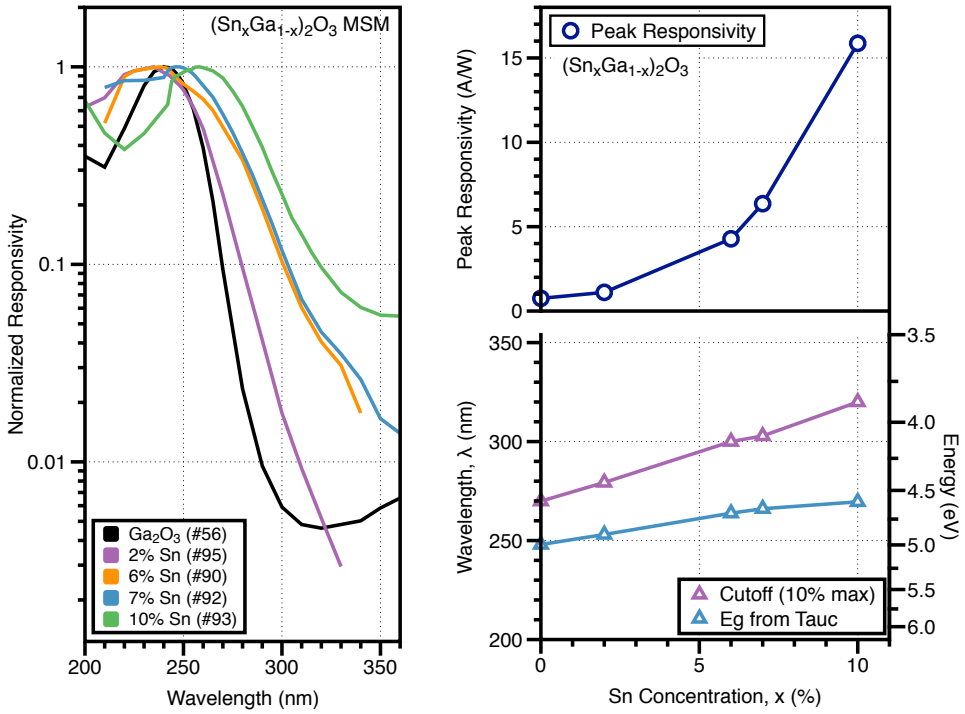

Figure 9: Photoresponse (left) of fabricated SGO MSM devices with varying Sn concentration. Right side of figure provides associated peak responsivity, wavelength of peak response, and the optical band gaps determined from Tauc plots for the epilayers.

Figure 9 provides a summary of the spectral responsivity data obtained from SGO MSM devices on sapphire with varying Sn concentrations. As noted in the top right of the figure, peak responsivity was found to systematically increase for higher Sn concentration in the epilayers, with the highest Sn concentration sample (10% Sn) demonstrating a peak responsivity of 15.9 A/W. Consistent with the transmission data from Task 1 used to determine the optical bandgap, the 10% cutoff wavelength of the devices was found to red shift to longer wavelengths as the Sn concentration was increased, as show in the bottom right of Figure 9.

Figure 10 provides the dependence of peak responsivity on applied bias for both Ga_2O_3 and SGO MSM devices.

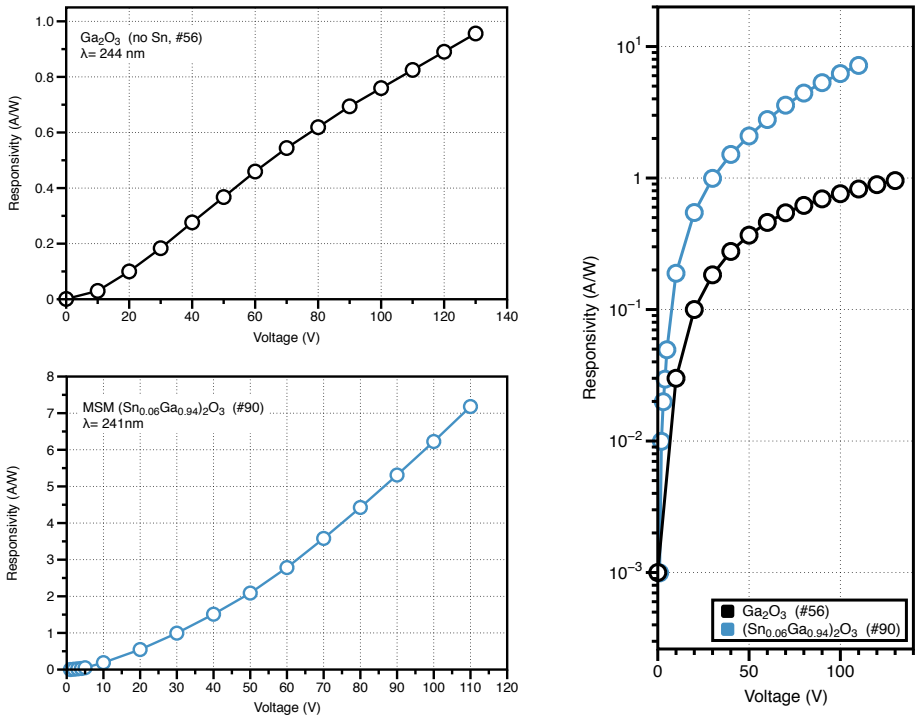

Figure 10: Peak Responsivity for Ga_2O_3 and SGO MSM Devices, demonstrating increased responsivity typically observed for SGO.

We observe a nearly linear increase in responsivity as a function of applied bias for both Ga_2O_3 and SGO MSM devices, with no abrupt changes over the measured range. For applied voltages up to around 60V the SGO MSM devices have a responsivity dependence that is slightly above a linear (see lower left graph in Figure 10), but then follow a linear increase for higher voltage levels. As has been observed during this project, the SGO epilayers result in a responsivity increase over pure Ga_2O_3 epilayers, as shown in the right of Figure 10.

Figure 11 (left) summarizes the temporal characteristics measured from the various SGO MSM devices with different Sn concentration. As Sn concentration is increased in the SGO, we observe a systematic shift to longer rise/fall times. The table in the right of the figure provides a summary of the rise and fall time constants found from fitting the data with a double exponential. We find that the τ_1 rise time constant shows a small increase, while the τ_2 rise time constant undergoes a major increase for increased Sn concentration. A similar observation was observed for the fall time as well. Given that the fast time constant (τ_1) is generally associated with band (Ev to Ec) transitions and the slow time constant (τ_2) relates to mid-gap trap-assisted recombination, we conclude that increasing Sn concentration results in a greater number of mid-gap traps in the SGO alloy, thus increasing the τ_2 time constants for both rise and fall times.

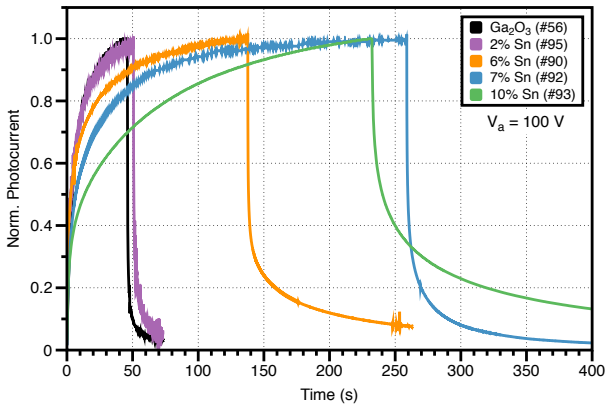

Sample	Rise (sec)		Fall (sec)		Peak Responsivity
	τ_1	τ_2	τ_1	τ_2	
Ga_2O_3 (#56)	3.05	15.39	0.221	3.39	0.751 A/W
x_{Sn}=0.02 (#95)	3.09	10.66	0.217	4.22	1.11 A/W
x_{Sn}=0.06 (#90)	3.04	35.06	0.690	31.09	4.28 A/W
x_{Sn}=0.07 (#92)	4.35	43.03	1.50	27.91	6.36 A/W
x_{Sn}=0.10 (#93)	4.10	78.86	16.34	191.23	15.87 A/W

Figure 11: Transient response characteristics of SGO MSM devices with varying Sn concentration. Right side of figure summarizes time constants for double exponential fit of rise and fall times.

Impact of Passivation on MSM Devices

While Schottky devices cover the entire active area of the detector with a semitransparent metal (Pt in our case), MSM samples have bare surfaces between the contact fingers that can be passivated. Given the high absorption coefficient for deep-UV light, most of the incident radiation is absorbed within the first ~100nm of the device (see next section on Schottky devices for a more extensive discussion). Thus, of interest is the potential impact of surface passivation on the device performance. While not a central focus of this STIR project, we did do a quick initial experiment to determine the impact of SiN passivation on the performance of a SGO MSM device. After fabrication and testing of a $(Sn_{0.06}Ga_{0.94})_2O_3$ MSM device (Sample #90), we deposited a 100nm SiN passivation layer over the entire surface of the device using PECVD. The sample was then re-measured, and results were compared with the initial measurements of the devices prior to passivation. A summary of the results in presented in Figure 12.

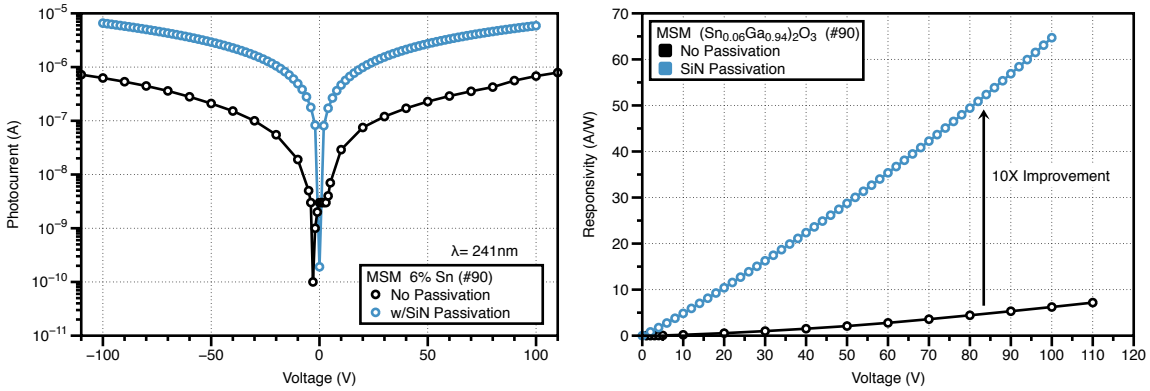

Figure 12: Impact of 100 nm SiN passivation layer on I-V (left) and responsivity (right) characteristics of 6% Sn SGO MSM device.

We found the SiN passivation layer to have a significant impact on the photocurrent of the device, increasing the peak responsivity by an order of magnitude, increasing the un-passivated responsivity of 6.22 A/W to 64.7 A/W after SiN passivation. Not shown in the figure is the dark current. We found the dark current to increase about 2 orders of magnitude when the SiN

passivation layer was put on the sample, but despite this increase, the 10x increase in responsivity (note this is after dark current subtraction) greatly outweighs the dark current increase. This demonstrates that passivation of such detectors should be looked at more closely in a systematic study to verify these initial results and better optimize the passivation design/material selection.

SGO on β-Ga_2O_3 (Schottky Devices)

One often overlooked item in UV-C detectors is the absorption depth within the material. Most materials have a relatively high absorption coefficient at short UV wavelengths, typically resulting in complete absorption of the UV light within the first 200-300nm. For Schottky devices, it is instructive to consider the depletion width in the semiconductor for a given metal and applied bias. We have calculated this for a Pt-Ga_2O_3 Schottky junction in Figure 13. The figure indicates the depletion width as a function of applied bias for various n-type doping concentrations. Superimposed in the figure is the optical intensity, ($I(x)/I_o$), as a function of depth in the Ga_2O_3, where I(x) is the intensity at a depth x (or x_d on the left axis), calculated for a wavelength of λ = 240nm.

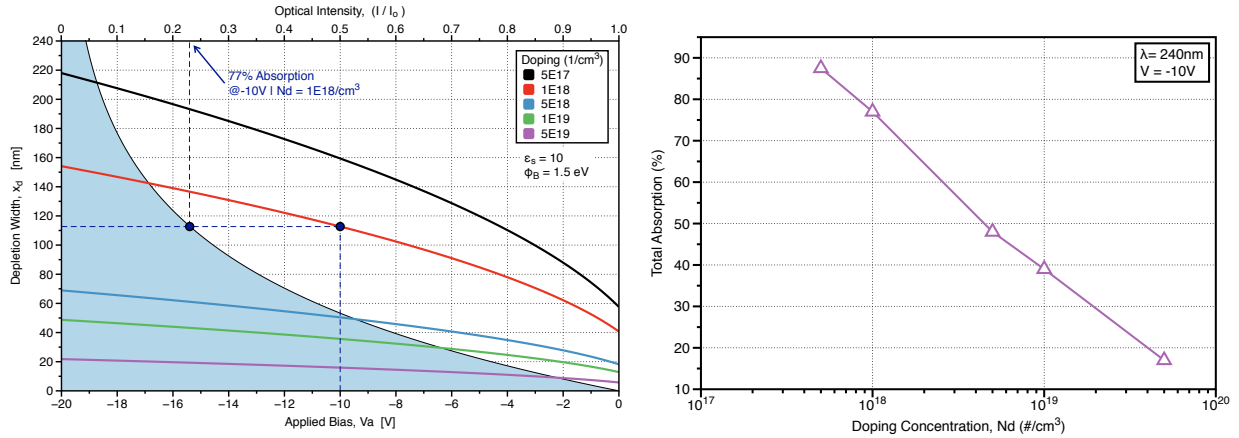

Figure 13: Calculated depletion width (left) as a function of applied bias for a Schottky device at different doping levels. Superimposed is the optical intensity of incident 240nm light at different depletion depth. The right side of the figure provides the total absorption as a function of doping concentration.

From the Figure 13 we can see that the optical intensity drops exponentially with depth, with ~ 90% of the light absorbed in the first 180 nm of the Ga_2O_3. We also find that the depletion width in the semiconductor varies from 20 nm to 220 nm, depending on both the reverse bias and doping in the material. Of the two, the doping has the greatest impact for most doping levels, with reverse bias having a lesser impact except for doping concentrations $<10^{18}/cm^3$. For β-Ga_2O_3 substrates, we expect doping levels to be in the low to mid-$10^{18}/cm^3$ range. This leads to several key points:

1) The depletion widths for n-type β-Ga_2O_3 substrates will generally range from 50-100 nm under typical reverse bias conditions.
2) The depletion width for unintentionally doped epilayers will generally be larger, ranging from 100-180 nm under typical bias conditions, due to their lower doping levels.
3) Based on these depletion widths, only 50-80% of the incident UV light will be absorbed in the depletion region with for n-type β-Ga_2O_3 substrates, and 70-90% for epitaxial layers.

4) There is an advantage for epitaxial layers with lower doping concentrations. This stems from the wider depletion width at a given reverse bias that allows for greater absorption of the incident light in the depletion zone, as plotted on the right side of Figure 13.

Initial testing of the Schottky devices included measurement of the current-voltage (I-V) characteristics with and without UV illumination. Figure 14 shows the typical I-V characteristics measured for the Schottky devices. In this case, the I-V data was taken in the dark and with UV illumination from the deuterium lamp incident on the device. The left side of the figure is a linear plot of data taken from a $(Sn_{0.15}Ga_{0.85})_2O_3$ device and the right side provides a comparison of result from the small (300μm) and large (500 μm) diameter devices.

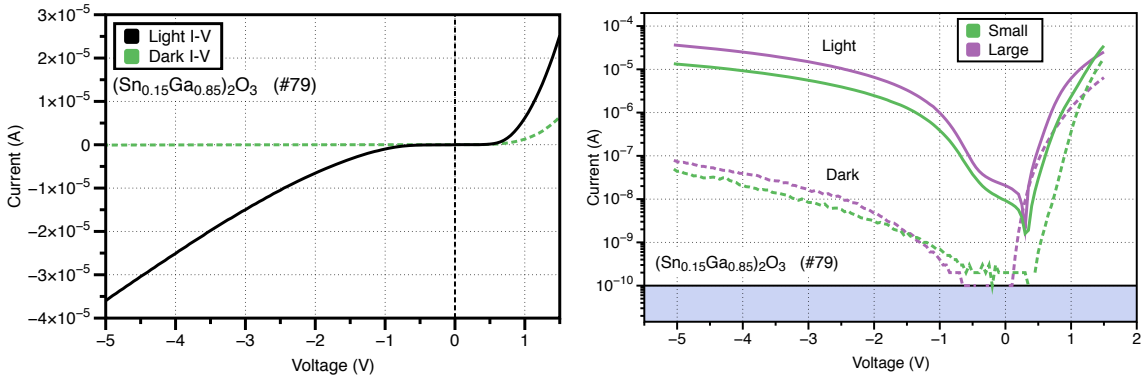

Figure 14: I-V characteristics for the Schottky devices, with and without UV illumination. Left side of the figure shows linear scale comparison of dark and light I-V for a large (500 μm) diameter device. Right side provides a comparison of the I-V characteristics small and large diameter devices.

The I-V characteristics follow the expected asymmetric behavior of a rectifying Schottky type device. The dark current is found to be in the pA regime for all samples, hitting the detection limit of our system, offering an attractive noise floor that is competitive with other UV detectors. When illuminated with UV light, the devices show a strong increase in current, that increases with increased reverse bias. In the logarithmic scale plot (Figure 14, right) we observe that the larger diameter device has a slightly higher dark current, as expected, but also an increased photocurrent generation, primarily due to the larger area of the device (note that the UV illumination spot size is larger than the device area).

We then tested the devices for spectral responsivity. Figure 15 (left) shows the responsivities for three different $(Sn_xGa_{1-x})_2O_3$ Schottky detectors with varying Sn concentration from 10% to 30%. As observed for MSM devices on sapphire, we find the peak responsivity wavelength to red shift for increased Sn concentration, accompanied by a large increase in peak responsivity, as shown in the right side of Figure 15.

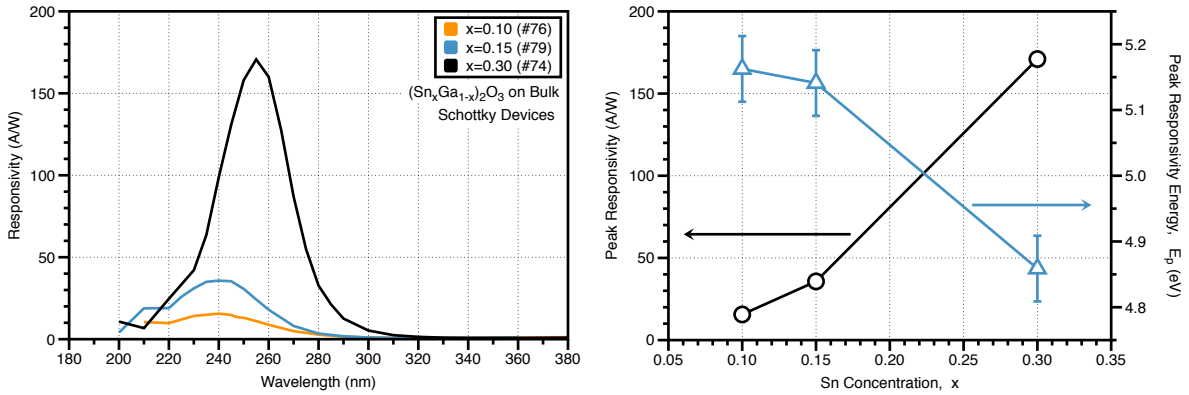

Figure 15: Spectral responsivity (left) for various Sn concentration SGO Schottky detectors, and dependence of peak responsivity and peak response energy as a function of Sn concentration (right).

Typically, we observe a trade-off between responsivity and temporal characteristics of UV detectors, primarily due to photoconductive gain mechanisms that impact both. Photoconductive gain generally increases as the number of trap sites increases in a device, leading to a greater number of electron injections per trapped photogenerated hole. The same trapping generally leads to slower rise and fall times for the UV detector.

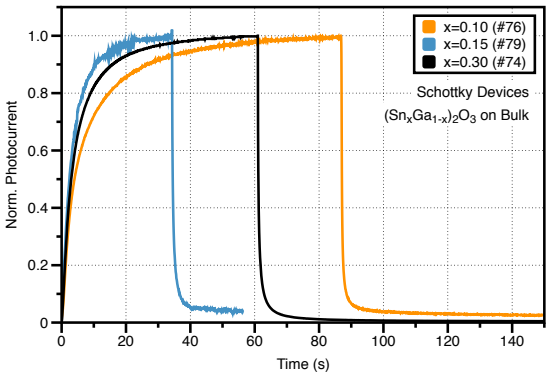

Sample	Rise (sec)		Fall (sec)		Peak Responsivity
	τ_1	τ_2	τ_1	τ_2	
x_{Sn}=0.10 (#76)	2.89	17.44	0.34	14.12	15.6 A/W
x_{Sn}=0.15 (#79)	2.69	8.71	0.26	1.59	35.7 A/W
x_{Sn}=0.30 (#74)	2.69	11.88	0.36	3.65	170.7 A/W

Figure 16: Temporal characteristics of SGO Schottky devices. Left side shows temporal data for devices with varying Sn concentration. Right side provides a table of double exponential fitted rise and fall time along with peak responsivity.

The temporal characteristics of Schottky devices based on SGO epilayers of different Sn concentration are provided in Figure 16. The left side of the figure shows the raw data for three different samples. All samples appear to qualitatively have similar rise and fall times irrespective of Sn concentration. Each was fitted with a double exponential to determine the τ_1 and τ_2 times for both the rise and fall segments. The basic equation is as follows

$$I(t) = I_o + Ae^{-\frac{(t-to)}{\tau_1}} + Be^{-\frac{(t-to)}{\tau_2}}$$

where *A* and *B* are scaling constants, *t* is time, and τ_1 and τ_2 are the fast and slow decay constants, respectively. The table in the right of Figure 16 summarizes the results of the fitting. As expected, variation in the τ_1 values for the rise and fall time of the samples are nearly identical, suggesting that for these SGO devices there is no major dependence of temporal characteristics on Sn concentration. We do see some variation in the τ_2 values, but this is also limited, suggesting the

samples are very similar. Despite the similarity of temporal characteristics, we find significant variation in the peak responsivity of the samples, with higher Sn concentrations leading to significant increases in the peak responsivity. This is particularly interesting since it does not follow the general trend noted above of a tradeoff between responsivity and temporal response.

Improved Growth Conditions and Resultant Impact

Near the end of the STIR project we transitioned to a dual zone Gallium effusion cell in an attempt to improve the Ga flux and epilayer quality. This section provides a summary of the results we obtained for both sapphire and bulk β-Ga_2O_3 substrate SGO films/devices.

Improved MSM Devices (on Sapphire)

Mid-way through the STIR project, we decided to make a transition to a dual zone Ga effusion cell for growth. This cell was put on the MBE system and we proceeded to optimize growth conditions for Ga_2O_3. This section provides a summary of the results we obtained using the improved growth conditions.

Figure 17 (left) provides a comparison of the responsivity of MSM devices for β-Ga_2O_3 (*no Sn*) epilayers on sapphire substrates, using standard growth and the improved growth using the dual zone cell.

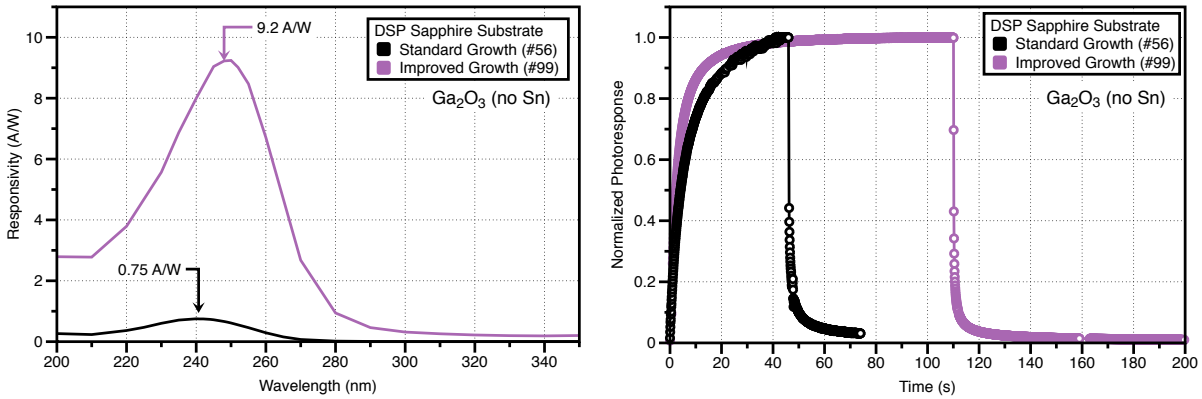

Figure 17: Comparison of responsivity (left) and temporal response (right) of Ga_2O_3 epilayers on DSP sapphire grown with standard and improved growth.

As is clearly demonstrated by the figure, we found the peak responsivity of the devices to increase by about an order of magnitude, from 0.75 A/W to 9.2 A/W, for the improved growth. This is a significant increase over our prior results, reaching an EQE value of 4.6×10^3 %. The right side of Figure 17 compares the temporal response of the samples. The improved growth also results in a significant improvement in the temporal response of the device, summarized in Table 1.

Table 1: Summary of temporal characteristics for Ga_2O_3 epilayers using standard and improved growth.

	Rise		Fall		Peak
Sample	τ_1 (s)	τ_2 (s)	τ_1 (s)	τ_2 (s)	**Responsivity**
Standard Growth (#56)	3.05	15.39	0.221	3.39	0.75 A/W
Improved Growth (#99)	2.53	13.86	0.157	3.87	9.2 A/W

We find the τ_1 and τ_2 time constants to slightly improve in tandem with a significant increase (>10x) in responsivity. This is significant since it verifies that the increased responsivity does not result in a temporal performance penalty, but actually offers major improvements to *both* the peak responsivity and temporal response in tandem.

As the natural next step, we then moved towards SGO epilayers on sapphire to determine the maximum obtainable responsivity with the improved growth. Figure 18 (left) provides a summary of the transmission comparison between the β-Ga_2O_3 and SGO epilayers using the improved growth.

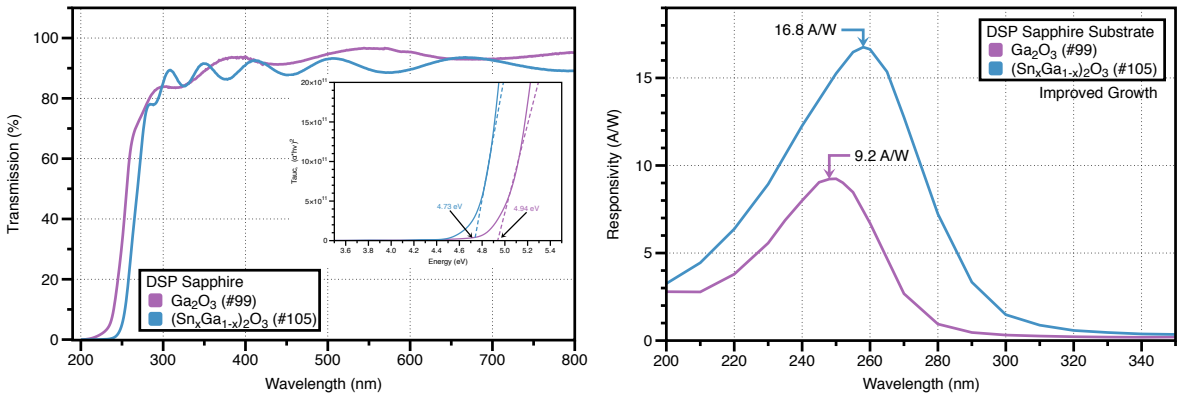

Figure 18: Comparison of transmission (left) and responsivity (right) for SGO and β-Ga_2O_3 epilayers on sapphire using improved growth. Inset on left side shows Tauc plot and resultant optical band gap position.

As with the prior standard growth, incorporation of Sn in the epilayer is found to shift the absorption edge to longer wavelengths. The inset shows the Tauc plots for the two epilayers, demonstrating the red shift in energy gap from 4.94 eV to 4.73 eV – we estimate a Sn concentration in the SGO layer of ~ 10%. The right of Figure 18 provides a comparison of the responsivity for the two samples. As was observed before (see Figure 9), incorporation of Sn into the Ga_2O_3 results in a red shift of the peak responsivity position and cutoff wavelength of the devices, as well as an increase in the peak responsivity.

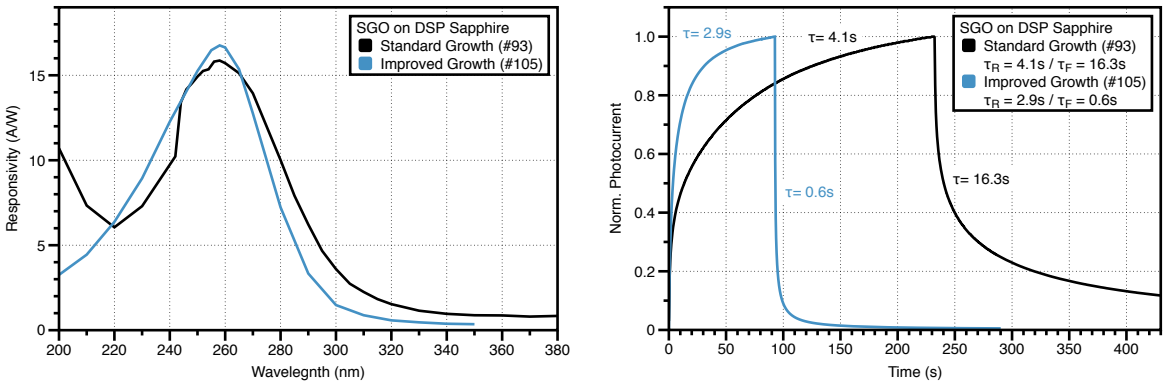

Figure 19: Comparison of SGO MSM devices from standard and improved growth. Left side of figure provides the measured responsivity and the right side shows the temporal characteristics.

Figure 19 compares two SGO MSM devices from epilayers grown with the standard and improved growth. Responsivity is found to increase slightly for the improved growth device as demonstrated on the left side of the figure. A more significant change is observed for the τ_1 values for the rise and fall time in the temporal data on the right of Figure 19. The improved growth shows a 25% reduction in the rise time constant, and a 96% drop in the fall time constant.

Improved Schottky Devices (on Bulk β-Ga_2O_3)

To verify the impact of Sn incorporation, we compared the transmission of the β-Ga_2O_3 substrate with an epilayer of SGO on top of a β-Ga_2O_3 substrate. The comparison is shown in Figure 20.

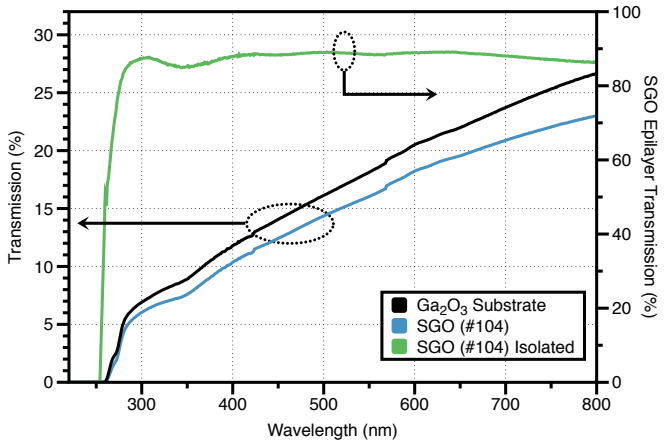

Figure 20: Comparison of transmission between an as-received β-Ga_2O_3 substrate and one with an SGO epilayer (black and blue curves, respectively). The backside roughness complicates the transmission data, but one can isolate the transmission of the SGO epilayer by normalizing it with the β-Ga_2O_3 data.

The transmission data from the two compared samples is complicated by the surface roughness of the backside of the β-Ga_2O_3 substrate since it is single side polished. As a result, isolation of the transmission properties of the SGO epilayer must be done by normalizing the data using that from the β-Ga_2O_3 substrate. The green curve in Figure 20 shows the results obtained from normalization, indicating the band edge has shifted towards a wavelength greater than 250nm due to the Sn incorporation.

Figure 21 (top) compares the measured spectral responsivity of SGO Schottky devices for the standard and improved growth. Note that the standard growth data has been multiplied by 100x in order to make it more visible in the figure. We find that the improved growth results in more than two orders of magnitude increase in spectral responsivity, increasing from 35.7 A/W to 11,532 A/W at -5V in the case shown.

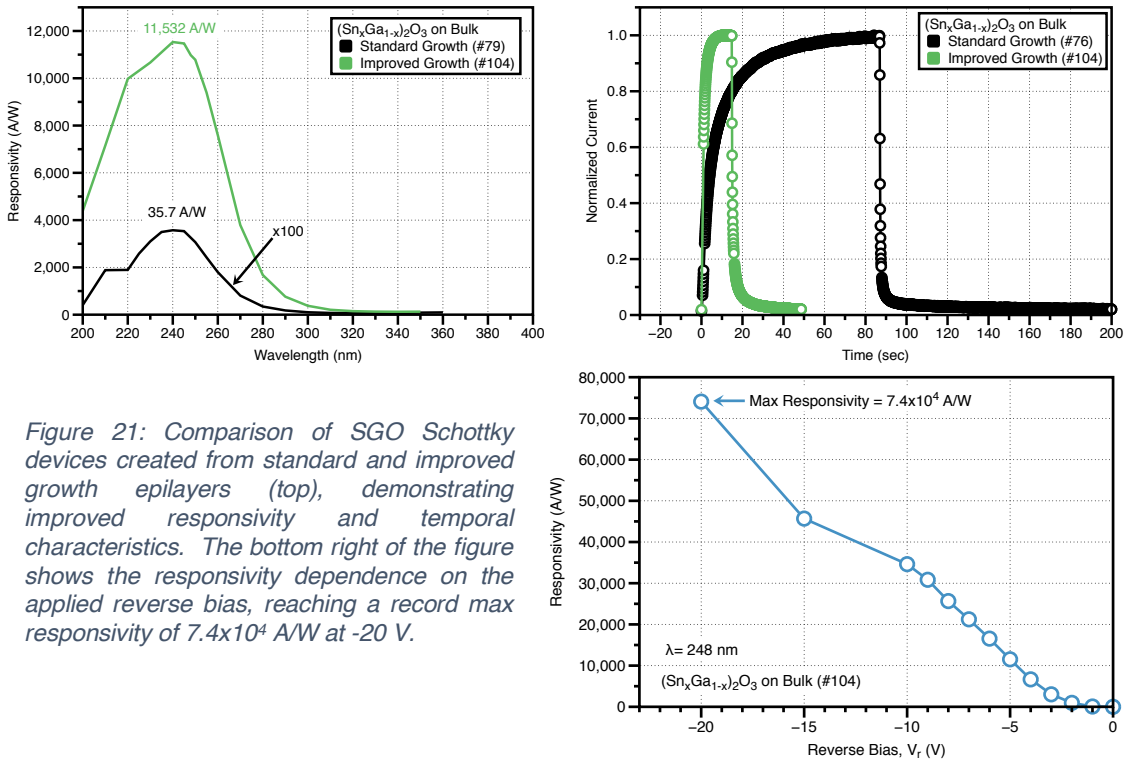

Figure 21: Comparison of SGO Schottky devices created from standard and improved growth epilayers (top), demonstrating improved responsivity and temporal characteristics. The bottom right of the figure shows the responsivity dependence on the applied reverse bias, reaching a record max responsivity of 7.4x10⁴ A/W at -20 V.

Equally impressive is the comparison of the temporal characteristics, plotted in the top right of Figure 21. We find that the improved growth increased the response speed of the device, with rise and fall times, determined from a double exponential fit, provided in Table 2.

Table 2: Summary of temporal characteristics for Ga_2O_3 epilayers using standard and improved growth.

Sample	Rise		Fall		Peak Responsivity
	τ_1 (s)	τ_2 (s)	τ_1 (s)	τ_2 (s)	
Standard Growth (#76)	2.89	17.44	0.337	14.12	35.7 A/W
Improved Growth (#104)	0.852	2.31	0.301	3.37	11,532 A/W

Comparison of Best Results

The following section provides a comparison of the results achieved in this STIR project with those of our prior work on other Army sponsored projects. Prior work focused on MgZnO based UV-detectors where we demonstrated MSM detectors based on wurtzite (w), cubic (c), and mixed phase (mp) epilayers. Figure 22 (left) provides a normalized summary of spectral responsivity characteristics for these detectors and those demonstrated under this STIR project. While peak responsivity positions vary slightly across the 230 – 260nm region, there are significant differences in their absolute values.

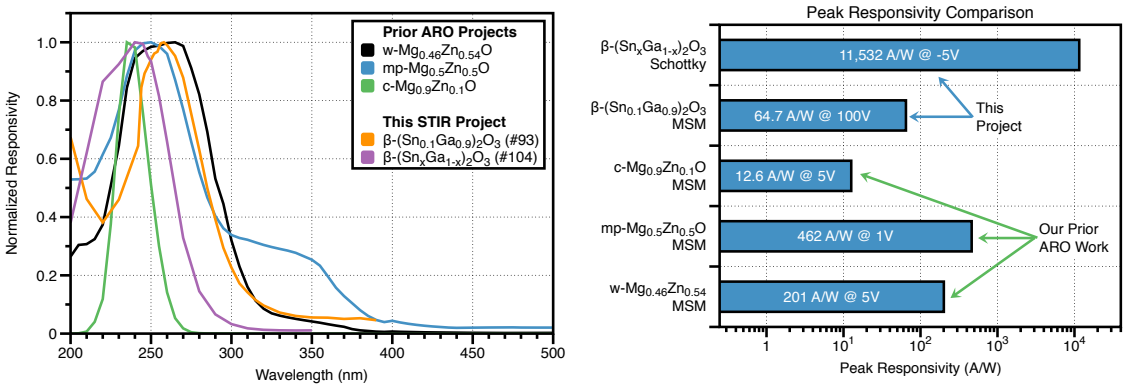

Figure 22: Comparison of results from this project with our prior ARO sponsored results for UV Detectors. Left side shows normalized responsivity and right side provides the peak responsivities achieved.

Peak responsivity values are compared in the right of Figure 22 - note that the Peak Responsivity in the x-axis is on a log scale due to the large differences between devices. For MSM devices, we find that SGO based devices are competitive over c-MgZnO MSM, and somewhat comparable to mp-MgZnO MSM devices if one considers that we can get an order of magnitude increase in responsivity by SiN passivation (see earlier results on passivation), though we note that mp-MgZnO MSM devices are not solar blind. More significantly, ***our SGO Schottky devices out-perform all other reported devices (see Appendix 1) by more than an order of magnitude, realizing record setting peak responsivity and EQE for all planar epilayer-based UV detectors we are aware of***. This includes consideration of all nitride and oxide-based UV detectors. The only reported responsivity higher than we have demonstrated here is that from a back-gated FET based on a micro-flake[11]; however, the device size is on the order of only 3 μm x 10 μm, and thus would result in a very weak signal that is two orders of magnitude smaller than ours since its capture cross-section of incident UV radiation is ~6,500 times smaller than our standard 500 μm diameter Schottky detector.

A summary of the best MSM and Schottky device samples demonstrated in this project are summarized in Table 3 below.

Table 3: Summary of best results obtained for the various sample types and device structures under this project.

Growth	Device Structure	Device	Peak Response WL	Dark Current	Response Time (τ_R / τ_F)	Responsivity
Standard	β-Ga_2O_3/Sapphire (#56)	MSM	240 nm	50 pA @ 10V	3.05 s / 0.22 s	0.75 A/W @ 100V
	SGO/Sapphire (#93)	MSM	258 nm	2 nA @ 10V	4.10 s / 16.34 s	15.9 A/W @ 100V
	SGO/Sapphire (#90) w/SiN	MSM	245 nm	3.8 nA @ 10V	3.04 s / 0.69 s	64.7 A/W @ 100V
	SGO/β-Ga_2O_3 (#74)	Schottky	255 nm	500 pA @ -5V	2.89 s / 0.34 s	170 A/W @ -5V
Improved	β-Ga_2O_3/Sapphire (#99)	MSM	248 nm	16 pA @ 10V	2.53 s / 0.16 s	9.2 A/W @ 100V
	SGO/Sapphire (#105)	MSM	258 nm	17 pA @ 10V	2.91 s / 0.61 s	16.8 A/W @ 100V
	SGO/β-Ga_2O_3 (#104)	Schottky	245 nm	750 nA @ -5V	0.85 s / 0.30 s	11,571 A/W @ -5V

Conclusions

Under the STIR project we successfully demonstrated the ability to tune the cut-off wavelength of $(Sn_xGa_{1-x})_2O_3$ detectors in the UV-C spectral region by adjusting the Sn concentration in the samples. Both MSM and Schottky based detectors were demonstrated, with the best performance of 11.5 kA/W being demonstrated from a SGO Schottky device at -5 V, equating to an EQE of nearly 60,000. This represents a record result when compared to planar Ga_2O_3 UV detectors reported in the literature to date.

Many questions remain, including the fundamental physics that leads to the extraordinarily high EQE (i.e. specific gain mechanism), what maximum responsivity is possible with further growth improvements and passivation, and how performance is impacted and can be optimized through device design. This STIR project was highly successful and met all of its designed goals, providing significant justification for further work on UV detectors utilizing Ga_2O_3-based compounds.

Appendix 1: Summary of UV Detector Performances

Material	Device	Method	Electrodes	Detection WL	Dark Current	Rejection Ratio	Responsivity	Response Time	Reference
GaN	MSM	MOCVD	Ni/Au	300-400nm	10pA @ 10V		50-150 A/W @ 6-15V		[12]
GaN	MSM	MOCVD	Ni/Au	365nm	80pA @ 2V	4.3	1.45 A/W		[13]
GaN	Schottky	MOCVD	Ni/Au	360nm			0.29 A/W @ -14V		[14]
GaN	Schottky (dual mode)	HVPE	Ni/Au	365nm	0.5pA @ -5V	6000 @ -5V	4.6 A/W @ -5V	46µs fall @ -5V	[15]
GaN	PIN	MOCVD	Ti/Al	365nm	20pA @ 5V	6700 UV/vis	0.23 A/W @ 5V	14 fs rise	[16]
GaN	PIN	MOCVD	Ni/Au	360nm	1pA @ -10V	2.16E4(@0V), 2870(@ -8V)	0.17 A/W		[17]
AlGaN	MSM		Ni/Au	222nm	<1pA @ 100V	5	0.12 A/W @ 20V		[18]
AlGaN	MSM	MOCVD	Ni or Mo	260nm	1nA @ 20V	2 orders (?)	0.1 A/W @ 250nm	20 ps	
AlGaN	PIN	MOVPE	Ti/Al/Ti/Au	365nm	50nA @ >100V	5	70 A/W @ 100V	6ms	[19]
AlGaN/GaN	MQW PIN	MOCVD		246nm			0.19 A/W		[20]
ZnO	MSM		Au				$2.6x10^3$ A/W @ 8V		[21]
ZnO (substrate)	Schottky	Hydrothermal	Pt (TC)/Au, Al (Ohmic)	365nm			0.185 A/W (Zinc face), 0.09 A/W (Oxygen face)		[22]
MgZnO	MSM	MOCVD	Au	238nm	16pA @ 15V	UV/Vis=4	0.129 A/W @ 15V	0.6ms (rise)/1.67µs (fall)	[23]
MgZnO	PN	PE-MBE	In, Ni/Au	330nm	30nA @ -5V	UV/Vis=2	2.16 mA/W (back ill.) @ -5V		[24]
MgZnO	MSM	RF-Sputtering	Au	290nm	3pA @ 5V	UV/Vis>4	10.5 mA/W @ 5V		[25]
MgZnO	APD (Schottky)	PA-MBE	Au	315nm	23 µA @ 12V		0.18 A/W@2V, 1,000A/W@31V	63.8ns (rise) / 1.2µs (fall)	[26]
NiMgO	MSM	MBE		250nm	<25nA	DUV/Vis=800	12mA/W	0.56s (rise)/7.10s(fall)	[27]
TGO	MSM	Laser MBE	Ti/Au	254nm	10nA @ 50V		30.5 mA/W	12.5s (rise) / 2.71s (fall)	[28]
SnO_2/Ga_2O_3	Schottky APD	Cation Exchange	In, Ti/Au	254nm	0.1nA @ -5V	7.40E+03	2,300 A/W @ 5.5V in gain mode (Not accurate because seems to indicate device size is ~ $5µm^2$)	48µs (rise)/ 100 µs (fall)	[29]
Ga_2O_3	Schottky	Nanobelts by CVD	Au	250nm	0.1pA @ 10V		851 A/W @250nm	< 0.3sec (not measurable)	[30]
Ga_2O_3 Nanosheet	Schottky MSM	Oxidized Exfoliated GaSe	Cr/Au	254nm	< 1nA @ 10V		3.3 A/W @ 254nm		[31]
Ga_2O_3							17 A/W @ 255nm		[32]

Material	Device	Method	Electrodes	Detection WL	Dark Current	Rejection Ratio	Responsivity	Response Time	Reference
Ga_2O_3/Sapphire	Ohmic MSM	MBE	Ti/Au (50nm/100nm)		1.4nA @ 10V	77 (254nm/265nm)	0.037 A/W @ 254nm		[33]
Ga_2O_3/p-Si	Schottky	Laser MBE	Ti/Au Top	254nm	30nA @ -3V		370 A/W @ 254nm	1.79s (rise) / 2.72s (fall)	[34]
Ga_2O_3	MSM	Nanobelts by CVD	Cr/Au	250nm			37.6 A/W @250nm	31s (rise) / 1.5s (fall)	[35]
Ga_2O_3	Back-gated FET	Exfoliated Flake		254nm	7.75 µA @ -30V	2.93 (254/365)	$1.8x10^5$ A/W @ 254nm		[11]
ZnO/α-Ga_2O_3	Schottky	Laser MBE	Au Top / Indium back	254nm	1pA @ -15V / 10nA @ -35V	10^3 (230nm/450nm), but dual band at 350nm	0.5A/W @ 230nm (-5V) / $3x10^3$ A/W at -35V in Avalanche	τ_1=563µs and τ_2=12.2ms for fall time	[36]
β-Ga_2O_3/ZnO	Schottky	RF Mag Sputtering	Ti/Au / In	254nm	0.3nA @ 0V		0.35 A/W	τ_1=0.62s / τ_2=7.84s (fall)	[37]
β-Ga_2O_3/SiC	HJ	Laser MBE	Au-Graphene	254nm	500pA		0.18 A/W	0.65s,7.8s (rise) / 1.73s, 15.22s (fall)	[38]
β-Ga_2O_3	MSM	PLD	Ni/Au	250nm	390pA @ 5V	7867 (UV/Vis)	0.903 A/W @ 250nm	>3s	[39]
β-Ga_2O_3-NSTO	HJ		Ti/Au / In	254nm	40nA @-10V		43.31 A/W @ -10V/254nm	0.07s (fall)	[40]
Amorph-Ga_2O_3	MSM	RF Mag Sputtering	ITO	280nm	0.3µA @ 10V		0.19 A/W	τ_1=19.1µs / τ_2=80.7µs (fall)	[41]
Au/ β-Ga_2O_3	Thermal Oxidation	Nanowire array	Au Schottky / Ga Ohmic	254nm	10pA @ -30V	38 (258nm/400nm)	$6x10^{-4}$ A/W	64µs (fall)	[42]
ZnO/ β-Ga_2O_3	HJ APD	CVD Core-shell MW	In (top) / Ti/Au (bottom)	254nm	100pA @ -6V	5x10^3 (250nm/400nm)	1,300 A/W @ -6V	20µs (rise) / 42µs (fall)	[43]
ZnO/ β-Ga_2O_3	HJ	CVD Core-shell MW	In (top) / Ti/Au (bottom)	251nm	>10pA @ -1V	690 (251nm /400nm)	$9.7x10^{-3}$ A/W @ 251nm	100µs (rise) / 900µs (fall)	[44]
β-Ga_2O_3 / Sapphire	MSM	MBE	Ni/Au	248nm	16pA @ 10V		9.2 A/W @ 100V	2.5s (rise) / 0.16s (fall)	**This Project**
$(Sn_xGa_{1-x})_2O_3$ / Sapphire	MSM	MBE	Ni/Au	258nm	17pA @ 10V		16.8 A/W @ 100V	2.9s (rise) / 0.61s (fall)	**This Project**
$(Sn_xGa_{1-x})_2O_3$ / Sapphire w/SiN	MSM	MBE	Ni/Au	245nm	3.8nA @ 10V		64.7 A/W @ 100V	3.04s (rise) / 0.69 (fall)	**This Project**
$(Sn_xGa_{1-x})_2O_3$ / β-Ga_2O_3	Schottky	MBE	Pt/Ni/Au (Top) Ti/Al/Ni (Back)	245nm	750nA @ -5V		11,571 A/W @ -5V	0.85s (rise) / 0.30s (fall)	**This Project**

Appendix 2: Summary of Epitaxial Samples Grown for this Project

Sample No	Epilayer by MBE	T_G (°C)	T_{Ga} (°C)	T_{Sn} (°C)	Sn%	GR (nm/hr)	BG (eV)	Device Fab	Remarks
SSP Sapphire Substrate Growths									
55	LT Ga_2O_3 nucleation layer followed by thick HT Ga_2O_3	700	930	--	--	35	5 – 5.1	--	RMS:4.42nm; Testing Ga flux
56		″	910	--	--	25	″	MSM	RMS:4.1nm; Lower Ga than prev
57		″	890	--	--	18	″	--	RMS:0.5nm; lower Ga than prev
58		750	890	--	--	26	″	--	RMS:2.7nm; Lower Tsub
59		″	910	--	--	22	″	--	RMS:2.5nm; same as #56, low Tsub
60		″	930	--	--	--	″	--	Same as #55 low Tsub
61	No NL	″	″	--	--	39	″	--	RMS:1.2nm; No NL but same as prev
62	HT thin NL	″	950	--	--	47	″	--	RMS:4.6nm; put very high Ga flux
63	″	″	″	690		50	″	MSM	RMS:4.3nm; Introduced Sn flux
64	″	600	930	″		47	″	″	RMS:1.5nm; Same Sn, low Ga flux
65	″	500	″	710		45	5.00	″	Low Tsub and high Sn flux
66	″	″	″	750	11.5	--	4.60	″	High Sn incorporation
67	″	″	″	″	--	--	--	--	Oxygen plasma deficient;
69	″	″	″	800	2.2	--	4.90	″	Higher Sn flux
70	″	″	″	850	--	--	4.86	″	Higher Sn flux but limited by Ga flux
94	HT Ga_2O_3 NL	700	900	800	--	--	4.90	--	Same as #93 but high Tsub, lower Sn incorporation than #93
DSP Sapphire Substrate Growths									
85	Graded growth. HT Ga_2O_3 NL followed by LT graded SnGaO	500	930 - 860	690 – 800	15	35	4.57	MSM	TGa decreases from 930°C & TSn increases from 700°C at same rate up to 860°C and 800°C respectively
86	No NL	″	850	800	6	25	4.78	″	1. Trying high Sn incorporation by reducing Ga flux 2. Discovered sufficient Ga on surface needed for Sn incorporation 3. Then adjust Sn% by varying Sn flux
87	NL	″	860	810	6	32	4.82	″	
88	No NL	″	860	730	4	20	4.78	″	
89	″	″	880	730	5	24.5	4.75	″	
90	″	″	900	730	6	24.8	4.70	″	Sufficient Ga flux
91	″	″	880	750	5	25	4.80	″	Insufficient Ga flux
92	″	″	900	750	7	24.8	4.66	″	Sufficient Ga flux
93	HT Ga_2O_3 NL	″	″	800	10	31.6	4.60	″	Sufficient Ga flux and higher Sn
95	″	″	″	700	2	34.6	4.90	″	Sufficient Ga flux and lowest Sn
96	Graded Sn flux only	″	910	800	3.4	--	--	″	Trying #85 with fixed TGa
97	No NL	″	900	800	10	--	4.60	″	Same as #93 without NL

Sample No	Epilayer MBE Notes	T_G (°C)	T_{Ga} (°C)	T_{Sn} (°C)	Sn%	GR (nm/hr)	BG (eV)	Device Fab	Remarks
99	No NL	750	950/910	--	--	53	5.00	MSM	Growth with modified Ga cell
100	″	500	1000/900	800	--	--	4.60	″	Different Ga/Sn flux ratio
101	″	″	″	830	--	--	″	″	
102	″	″	″	850	--	--	″	″	
103	″	″	960	780	--	--	″	″	Further Modified Ga cell
105	″	″	980	750	--	--	″	″	Different Ga/Sn flux ratio
Ga_2O_3 Substrate Growths									
74	Thick HT NL	600	930	690	--	--	--	Schottky	No-flash off; high Sn incorporation
75	″	″	″	720	--	--	--	″	Regular Flash off
76		″	″	750	--	--	--	″	Higher Sn flux
77	″	″	″	660	--	--	--	″	Lowest Sn flux
78	″	″	″	700	--	--	--	″	Higher Sn flux than prev
79	″	″	″	780	--	--	--	″	Very high Sn cell temp
104	No NL	″	980	830	--	--	--	″	Lower Plasma power than usual. Modified Ga cell than prev batch
106	″	″	″	800	--	--	--	″	Different Ga/Sn flux ratio though TSn is same
107	″	″	″	800	--	--	--	″	

Abbreviations:

SSP: Single Side Polished
DSP: Double side Polished
NL: Nucleation Layer
GR: Growth Rate
BG: Band Gap
MSM: Metal-Semiconductor-Metal
HT: High Temperature
LT: Low Temperature

Bibliography

[1] A. Ohtomo *et al.*, "MgxZn1-xO as a II-VI widegap semiconductor alloy," (in English), *Applied Physics Letters,* vol. 72, no. 19, pp. 2466-2468, May 11 1998.

[2] V. Kuryatkov *et al.*, "Solar-blind ultraviolet photodetectors based on superlattices of AlN/AlGa(In)N," (in English), *Applied Physics Letters,* vol. 82, no. 9, pp. 1323-1325, Mar 3 2003.

[3] M. Higashiwaki *et al.*, "Recent progress in Ga2O3 power devices," (in English), *Semiconductor Science and Technology,* vol. 31, no. 3, Mar 2016.

[4] M. Y. Tsai, O. Bierwagen, M. E. White, and J. S. Speck, "beta-Ga2O3 growth by plasma-assisted molecular beam epitaxy," (in English), *Journal of Vacuum Science & Technology A,* vol. 28, no. 2, pp. 354-359, Mar 2010.

[5] Y. Tomm, J. M. Ko, A. Yoshikawa, and T. Fukuda, "Floating zone growth of beta-Ga2O3: A new window material for optoelectronic device applications," (in English), *Solar Energy Materials and Solar Cells,* vol. 66, no. 1-4, pp. 369-374, Feb 2001.

[6] K. Akito, K. Kimiyoshi, W. Shinya, Y. Yu, M. Takekazu, and Y. Shigenobu, "High-quality β-Ga 2 O 3 single crystals grown by edge-defined film-fed growth," *Japanese Journal of Applied Physics,* vol. 55, no. 12, p. 1202A2, 2016.

[7] A. Hideo, N. Kengo, T. Hidetoshi, A. Natsuko, S. Kazuhiko, and Y. Yoichi, "Growth of β-Ga 2 O 3 Single Crystals by the Edge-Defined, Film Fed Growth Method," *Japanese Journal of Applied Physics,* vol. 47, no. 11R, p. 8506, 2008.

[8] Z. Galazka *et al.*, "On the bulk ß-Ga2O3 single crystals grown by the Czochralski method," (in English), *Journal of Crystal Growth,* vol. 404, pp. 184-191, Oct 15 2014.

[9] C. Janowitz *et al.*, "Experimental electronic structure of In2O3 and Ga2O3," (in English), *New Journal of Physics,* vol. 13, Aug 16 2011.

[10] X. Du *et al.*, "Preparation and characterization of Sn-doped ß-Ga2O3 homoepitaxial films by MOCVD," *Journal of Material Science,* vol. 50, pp. 3252-3257, 2015.

[11] S. Oh, J. Kim, F. Ren, S. J. Pearton, and J. Kim, "Quasi-two-dimensional β-gallium oxide solar-blind photodetectors with ultrahigh responsivity," *Journal of Materials Chemistry C,* vol. 4, no. 39, pp. 9245-9250, 2016.

[12] A. Müller *et al.*, "GaN membrane-supported UV photodetectors manufactured using nanolithographic processes," *Microelectronics Journal,* vol. 40, no. 2, pp. 319-321, 2009.

[13] A. Müller *et al.*, "Front and backside-illuminated GaN/Si based metal–semiconductor–metal ultraviolet photodetectors manufactured using micromachining and nano-lithographic technologies," *Thin Solid Films,* vol. 520, no. 6, pp. 2158-2161, 2012.

[14] D. Zhao *et al.*, "An anomalous gain mechanism in GaN Schottky barrier ultraviolet photodetectors," *Chinese Physics Letters,* vol. 26, no. 5, p. 058501, 2009.

[15] F. Xie, H. Lu, D. Chen, F. Ren, R. Zhang, and Y. Zheng, "Bias-Selective Dual-Operation-Mode Ultraviolet Schottky-Barrier Photodetectors Fabricated on High-Resistivity Homoepitaxial GaN," *IEEE Photonics Technology Letters,* vol. 24, no. 24, pp. 2203-2205, 2012.

[16] B. Butun, T. Tut, E. Ulker, T. Yelboga, and E. Ozbay, "High-performance visible-blind GaN-based p-i-n photodetectors," *Applied Physics Letters,* vol. 92, no. 3, 2008.

[17] H.-F. Lian *et al.*, "High Deep-Ultraviolet Quantum Efficiency GaN P—I—N Photodetectors with Thin P-GaN Contact Layer," *Chinese Physics Letters,* vol. 30, no. 1, 2013.

[18] M. Gökkavas, S. Butun, H. Yu, T. Tut, B. Butun, and E. Ozbay, "Dual-color ultraviolet metal-semiconductor-metal AlGaN photodetectors," *Applied Physics Letters,* vol. 89, no. 14, 2006.

[19] M. Martens *et al.*, "High gain ultraviolet photodetectors based on AlGaN/GaN heterostructures for optical switching," *Applied Physics Letters,* vol. 98, no. 21, 2011.
[20] A. Rostami, N. Ravanbaksh, S. Golmohammadi, and K. Abedi, "High-responsivity AlGaN-GaN multi-quantum well UV photodetector," *International Journal of Numerical Modelling: Electronic Networks, Devices and Fields,* vol. 27, no. 2, pp. 309-317, 2014.
[21] K. W. Liu *et al.*, "Ultraviolet photoconductive detector with high visible rejection and fast photoresponse based on ZnO thin film," *Solid-State Electronics,* vol. 51, no. 5, pp. 757-761, 2007.
[22] H. Endo *et al.*, "Schottky ultraviolet photodiode using a ZnO hydrothermally grown single crystal substrate," *Applied Physics Letters,* vol. 90, no. 12, 2007.
[23] S. Han *et al.*, "Photoconductive gain in solar-blind ultraviolet photodetector based on Mg0.52Zn0.48O thin film," *Applied Physics Letters,* vol. 99, no. 24, 2011.
[24] W. W. Liu *et al.*, "MgZnO/ZnO p–n junction UV photodetector fabricated on sapphire substrate by plasma-assisted molecular beam epitaxy," *Solid State Sciences,* vol. 12, no. 9, pp. 1567-1569, 2010.
[25] C. Li, Z. Zhang, H. Chen, X. Xie, and D. Shen, "Vertical MgZnO Schottky ultraviolet photodetector with Al doped MgZnO transparent electrode," *Thin Solid Films,* vol. 548, pp. 456-459, 2013.
[26] J. Yu, C. X. Shan, J. S. Liu, X. W. Zhang, B. H. Li, and D. Z. Shen, "MgZnO avalanche photodetectors realized in Schottky structures," *physica status solidi (RRL) - Rapid Research Letters,* vol. 7, no. 6, pp. 425-428, 2013.
[27] J. W. Mares, R. C. Boutwell, M. Wei, A. Scheurer, and W. V. Schoenfeld, "Deep-ultraviolet photodetectors from epitaxially grown NixMg1–xO," *Applied Physics Letters,* vol. 97, no. 16, 2010.
[28] X. Zhao *et al.*, "Growth and Characterization of Sn Doped β-Ga2O3 Thin Films and Enhanced Performance in a Solar-Blind Photodetector," *Journal of Electronic Materials,* vol. 46, no. 4, pp. 2366-2372, 2017.
[29] W. E. Mahmoud, "Solar blind avalanche photodetector based on the cation exchange growth of β-Ga2O3/SnO2 bilayer heterostructure thin film," *Solar Energy Materials and Solar Cells,* vol. 152, pp. 65-72, 2016.
[30] R. Zou *et al.*, "High detectivity solar-blind high-temperature deep-ultraviolet photodetector based on multi-layered (l00) facet-oriented beta-Ga(2)O(3) nanobelts," *Small,* vol. 10, no. 9, pp. 1848-56, May 14 2014.
[31] W. Feng *et al.*, "Synthesis of two-dimensional β-Ga2O3nanosheets for high-performance solar blind photodetectors," *J. Mater. Chem. C,* vol. 2, no. 17, pp. 3254-3259, 2014.
[32] G. C. Hu, C. X. Shan, N. Zhang, M. M. Jiang, S. P. Wang, and D. Z. Shen, "High gain Ga(2)O(3) solar-blind photodetectors realized via a carrier multiplication process," *Opt Express,* vol. 23, no. 10, pp. 13554-61, May 18 2015.
[33] T. Oshima, T. Okuno, and S. Fujita, "Ga2O3Thin Film Growth onc-Plane Sapphire Substrates by Molecular Beam Epitaxy for Deep-Ultraviolet Photodetectors," *Japanese Journal of Applied Physics,* vol. 46, no. 11, pp. 7217-7220, 2007.
[34] X. C. Guo *et al.*, "β -Ga 2 O 3 / p -Si heterojunction solar-blind ultraviolet photodetector with enhanced photoelectric responsivity," *Journal of Alloys and Compounds,* vol. 660, pp. 136-140, 2016.
[35] L. Li *et al.*, "Deep-ultraviolet solar-blind photoconductivity of individual gallium oxide nanobelts," *Nanoscale,* vol. 3, no. 3, pp. 1120-6, Mar 2011.
[36] X. Chen *et al.*, "Solar-Blind Photodetector with High Avalanche Gains and Bias-Tunable Detecting Functionality Based on Metastable Phase alpha-Ga2O3/ZnO Isotype

Heterostructures," *ACS Appl Mater Interfaces,* vol. 9, no. 42, pp. 36997-37005, Oct 25 2017.
[37] D. Y. Guo *et al.*, "Fabrication ofβ-Ga2O3/ZnO heterojunction for solar-blind deep ultraviolet photodetection," *Semiconductor Science and Technology,* vol. 32, no. 3, 2017.
[38] Y. Qu *et al.*, "Enhanced Ga 2 O 3 /SiC ultraviolet photodetector with graphene top electrodes," *Journal of Alloys and Compounds,* vol. 680, pp. 247-251, 2016.
[39] F.-P. Yu, S.-L. Ou, and D.-S. Wuu, "Pulsed laser deposition of gallium oxide films for high performance solar-blind photodetectors," *Optical Materials Express,* vol. 5, no. 5, 2015.
[40] D. Guo *et al.*, "Zero-Power-Consumption Solar-Blind Photodetector Based on beta-Ga2O3/NSTO Heterojunction," *ACS Appl Mater Interfaces,* vol. 9, no. 2, pp. 1619-1628, Jan 18 2017.
[41] S. Cui, Z. Mei, Y. Zhang, H. Liang, and X. Du, "Room-Temperature Fabricated Amorphous Ga2O3 High-Response-Speed Solar-Blind Photodetector on Rigid and Flexible Substrates," *Advanced Optical Materials,* vol. 5, no. 19, 2017.
[42] X. Chen *et al.*, "Self-Powered Solar-Blind Photodetector with Fast Response Based on Au/beta-Ga2O3 Nanowires Array Film Schottky Junction," *ACS Appl Mater Interfaces,* vol. 8, no. 6, pp. 4185-91, Feb 17 2016.
[43] B. Zhao *et al.*, "Solar-Blind Avalanche Photodetector Based On Single ZnO-Ga(2)O(3) Core-Shell Microwire," *Nano Lett,* vol. 15, no. 6, pp. 3988-93, Jun 10 2015.
[44] B. Zhao *et al.*, "An Ultrahigh Responsivity (9.7 mA/W) Self-Powered Solar-Blind Photodetector Based on Individual ZnO-Ga2O3 Heterostructures," *Advanced Functional Materials,* vol. 27, no. 17, 2017.